Journal of Photonics for Energy

PhotonicsforEnergy.SPIEDigitalLibrary.org

Analysis of bulk heterojunction material parameters using lateral device structures

Eric Danielson
Zi-En Ooi
Kelly Liang
Joshua Morris
Christopher Lombardo
Ananth Dodabalapur

SPIE.

REVIEW

Analysis of bulk heterojunction material parameters using lateral device structures

Eric Danielson,[a,b] Zi-En Ooi,[c] Kelly Liang,[a,d] Joshua Morris,[e,†] Christopher Lombardo,[f] and Ananth Dodabalapur[a,d,*]

[a]University of Texas at Austin, Microelectronics Research Center, Austin, Texas 78758
[b]University of Texas at Austin, Materials Science and Engineering Program, Austin, Texas 78712
[c]Institute of Materials Research and Engineering, Agency for Science, Technology and Research (A*STAR), 3 Research Link, Singapore 117602, Republic of Singapore
[d]University of Texas at Austin, Department of Electrical and Computer Engineering, Austin, Texas 78712
[e]University of Texas at Austin, Department of Chemistry and Biochemistry, Austin, Texas 78759
[f]Harvard School of Engineering and Applied Sciences, 29 Oxford Street, Cambridge, Massachusetts 02138

Abstract. We review the key optoelectronic properties of lateral organic bulk heterojunction (BHJ) device structures with asymmetric contacts. These structures are used to develop a detailed model of charge transport and recombination properties within materials used for organic photovoltaics. They permit a variety of direct measurement techniques, such as nonlinear optical microscopy and *in situ* potentiometry, as well as photoconductive gain and carrier drift length studies from photocurrent measurements. We present a theoretical framework that describes the charge transport physics within these devices. The experimental results presented are in agreement with this framework and can be used to measure carrier concentrations, recombination coefficients, and carrier mobilities within BHJ materials. Lateral device structures offer a useful complement to measurements on vertical photovoltaic structures and provide a more complete and detailed picture of organic BHJ materials. [DOI: 10.1117/1.JPE.4.040994]

Keywords: photovoltaic systems; organic materials; carrier dynamics.

Paper 14004 received Feb. 15, 2014; revised manuscript received Jun. 6, 2014; accepted for publication Jun. 9, 2014; published online Jul. 25, 2014.

1 Introduction

Organic photovoltaics (OPV) has attracted widespread attention and research as a promising renewable energy technology due to its low-cost, high-volume manufacturing potential and rapid advances in their power conversion efficiency of >11%.[1] Bulk heterojunctions (BHJs) are an important class of materials commonly used in OPV. BHJs are complex mixtures of an electron donating and an electron accepting organic semiconductors, phase separated at the nanometer scale. The photovoltaic performance of an organic BHJ material is highly dependent on its nanoscale morphology, which can be affected by a variety of factors, including the chemical structure of the organic semiconductors, the solvent and solvent additives, the fabrication methodology, and the environmental exposure. New measurement techniques and tools are needed to clarify the interaction between these factors affecting the morphology and the

*Address all correspondence to: Ananth Dodabalapur, E-mail: ananth.dodabalapur@engr.utexas.edu

†Present address: Georgia Institute of Technology, Department of Chemistry and Biochemistry, 901 Atlantic Drive, Atlanta, Georgia 30332.

materials' electronic properties, such as the carrier mobilities, charge concentrations, and recombination rate constants. To study these properties, researchers have typically utilized vertical solar cell structures similar to an actual OPV cell. A variety of techniques, including transient photocurrents,[2] photo-generated charge extraction in a linearly increasing voltage (photo-CELIV),[3] time-of-flight,[4,5] impedance spectroscopy,[6,7] time-resolved terahertz spectroscopy,[8] time-resolved microwave conductivity,[9] and dark-injection space charge limited current,[10] have been successfully employed by many research groups. To complement these studies, we have developed techniques that measure the transport and recombination properties of organic BHJs along the in-plane axis, or lateral direction. This paper will summarize some of the important insights that can be obtained through lateral BHJ measurement techniques.

A schematic diagram of a lateral BHJ device is shown in Fig. 1(a). The two electrodes are defined on the same plane, and the BHJ material can be spun or deposited from above. The photoactive region is defined by the channel between the two electrodes. This configuration is a poor geometry for OPV efficiency but is a useful platform for materials diagnostics. Key charge transport and recombination parameters in organic BHJ systems can be anisotropic. This is particularly true for some of the materials that are in use in high-efficiency solar cell devices. While values of these parameters along the direction of the charge transport in solar cells are especially important, it is also very useful to study the values of these parameters in a perpendicular direction. We note that while carrier densities and recombination coefficients are scalar quantities, their experimentally determined values depend on the direction of the charge flow during a measurement. It is, therefore, important to measure such parameters along multiple directions. Lateral BHJ devices allow for these types of measurements over a wide range of length scales (from tens of nanometers to hundreds of micrometers), are more amenable to device modeling due to their uniform photogeneration profile, and permit direct access to the active layer. In this review paper, we describe a variety of techniques to measure the photocurrent, potentiometry, and electric field strength within the device channel during operation. From correlations with transport simulations of lateral BHJ devices, we are able to calculate these key transport parameters of organic BHJ materials.

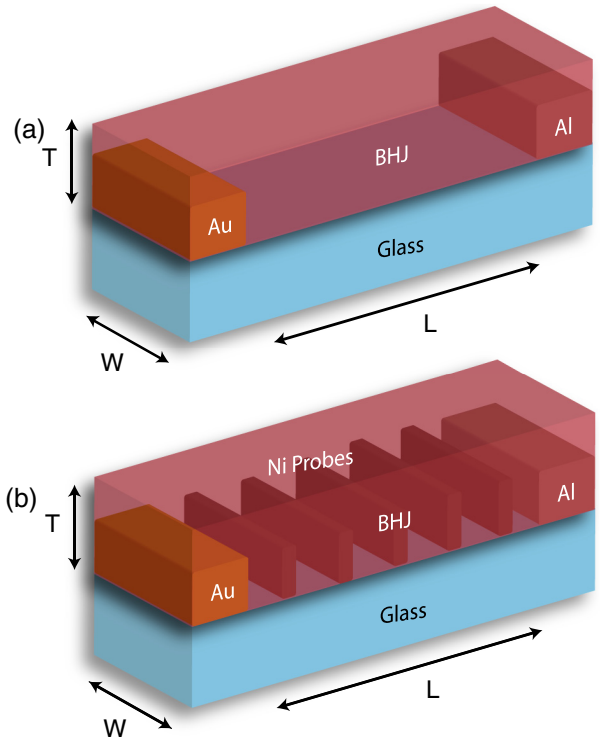

Fig. 1 A schematic illustration of a lateral bulk heterojunction (BHJ) device without (a) and with (b) *in situ* voltage probes.

2 Theory

Theoretical modeling of lateral BHJ devices under a large reverse voltage bias predicts space charge limited (SCL) transport behavior[11] that has been experimentally confirmed in previous studies.[12–14] Due to these large biases, large regions of space charge form adjacent to the electrodes even when the carrier mobilities are similar. If the mobilities are mismatched, the space charge region (SCR) dominated by the slower carrier grows in size while the other shrinks. Under a small or zero bias, these SCRs become comparatively small, particularly when the electron and hole mobilities are well balanced. At the channel lengths and biases we employ in our lateral BHJ devices, SCL transport is dominant, but we use this to analyze charge transport properties of the material. Although the bias voltages we employ are large, the value of the electric field in these structures is similar to that present in a typical vertical solar cell device. A theoretical treatment of SCL transport was first proposed by Goodman and Rose[15] and was first observed within OPV cells by Mihailetchi et al.[16] The ratio of charge carrier mobilities determines many features of a lateral BHJ charge transport and device operation. As stated above, when the two mobilities are similar, there is efficient carrier collection within a drift length of the two electrodes and a central region where virtually no photocurrent can be collected and all generated charge recombines [recombination zone (RZ)]. When there is a significant difference between the carrier mobilities, one SCR becomes very small, and the device can be considered to be divided into two transport zones: SCR and RZ. Theoretical simulations of these two cases have been previously presented by Ooi et al.[11] and Lombardo et al.[17]

These simulations are based on a device model that treats the organic BHJ as a composite semiconductor. Carriers are photogenerated homogenously across the device, independent of electric field strength. Charge carrier and electric field profiles of lateral devices are developed from a system of equations consisting of the drift-diffusion equation for electrons and holes, the steady-state continuity equation, and Poisson's equation for electrostatics.[11,18]

$$J_{\mathrm{ph},p} = e\mu_p p(x)E(x) - \mu_p kT\frac{dp(x)}{dx}, \tag{1}$$

$$J_{\mathrm{ph},n} = e\mu_n n(x)E(x) + \mu_n kT\frac{dn(x)}{dx}, \tag{2}$$

$$\frac{dJ_{\mathrm{ph},p}}{dx} = -\frac{dJ_{\mathrm{ph},n}}{dx} = eG - eR(x), \tag{3}$$

$$-\frac{d^2\phi}{dx^2} = \frac{e}{\varepsilon}[p(x) - n(x)], \tag{4}$$

where $J_{\mathrm{ph},n,p}$ are the photogenerated electron and hole current densities, $n(x)$ and $p(x)$ are the photogenerated electron and hole concentrations, $\mu_{n,p}$ are the electron and hole mobilities, φ is the electric potential, E is the electric field, G is the generation rate, and $R(x)$ is the recombination rate that is modeled as bimolecular. Electrical contacts in this device model are considered to be noninjecting and with no barrier for charge extraction. Carrier traps and trap-assisted recombination mechanisms are also not included in the model.

This model has been implemented using two approaches. First, a custom program that solves Eqs. (1) to (4) in one-dimension was written to generate carrier, potential, electric field, generation, and recombination profiles across a lateral BHJ device under illumination. This model assumed electron and hole mobilities that were constant with an electric field. Electric field dependence of these mobilities (which are known to possess Poole-Frenkel dependence[19,20]) was subsequently included as shown in Fig. 8. Second, a two-dimensional (2-D) software package from Silvaco (ATLAS®, Austin, Texas) was used in a one-dimensional mode as the second dimension was not found to be necessary for modeling. This model used bimolecular recombination and treated the carrier mobilities as field dependent with Poole-Frenkel behavior. Results from this model are described in Fig. 10. However, both approaches predicted the three-zone

behavior and variation in carrier concentrations, electric fields, and recombination across a lateral BHJ device described below.

Using our device model, the results from a numerical simulation of a three-zone lateral device is shown in Fig. 2. The simulation was run for a 20-μm lateral BHJ device using the parameters listed in Table 1, under one sun condition (100 mW/cm^2) and an applied bias of 1×10^5 V/cm. The anode [gold (Au)] is located at 0 μm and the cathode [aluminum (Al)] is located at 20 μm. The carrier concentrations as a function of position are shown in Fig. 2(a); the electric field and potential profile of the lateral BHJ device are shown in Fig. 2(b). The different regions can be distinguished from the changes in these parameters. In Fig. 2(a), areas adjacent to the electrodes accumulate charge carriers of one type: holes adjacent to the anode and electrons adjacent to the cathode. These areas are the SCRs, where carriers are transported into more quickly than they can be extracted.[15,17] SCRs also contribute the majority of the photocurrent and are separated by the RZ, in which all photogenerated carriers recombine. RZ has equal and high concentrations of electrons and holes, but these generated charges do not contribute to the photocurrent.

From these spatial plots, the extent of SCRs can be determined from multiple measurements. These measurements on size, voltage, and carrier concentrations within the SCRs can be used to calculate important charge transport parameters and characterize organic BHJ materials. The ratio of the size of the SCRs is directly proportional to the mobility ratio of their dominant carriers; therefore, in Fig. 2(a), the larger SCR is dominated by the slower carrier holes adjacent to the anode. As seen in Fig. 2(b), RZ has a small constant electric field, while SCRs have a larger electric field and a larger voltage dropped across them. The voltage drop across each SCR depends on its drift length λ and, therefore, on the carrier mobilities. To determine the relationship between the mobility ratio and the ratio between the SCR voltage drops, simulations using our one-dimensional model were run for a broad range of typical properties of organic BHJ films, such as photogeneration rates, recombination coefficients, and relative permittivities.[18] Under each of these different parameters, 11 pairs of ΔV_a and ΔV_c were recorded from 11 different combinations of electron and hole mobilities ranging from 10^{-4} to 10^{-3} cm^2/Vs. The resulting ratio of SCR voltages from these 198 simulations is plotted versus the mobility ratio in Fig. 3. Over this range of parameters, the mobility and voltage drop ratios follow an empirical power law. From the fits on Fig. 3, the relationship is best described by the following equation, although there is a narrow spread in the power values.

$$\left(\frac{\mu_n}{\mu_p}\right) = \left(\frac{\Delta V_a}{\Delta V_c}\right)^{0.46}, \tag{5}$$

where μ_n and μ_p are the electron and hole mobilities, and ΔV_A and ΔV_C are the voltage drops across the anode and cathode, respectively. This empirical formula provides a method to estimate the mobility ratio of an organic BHJ material from the voltage drops across the SCRs, which are easier to measure than the SCR widths. The voltage drops can be measured from potentiometry

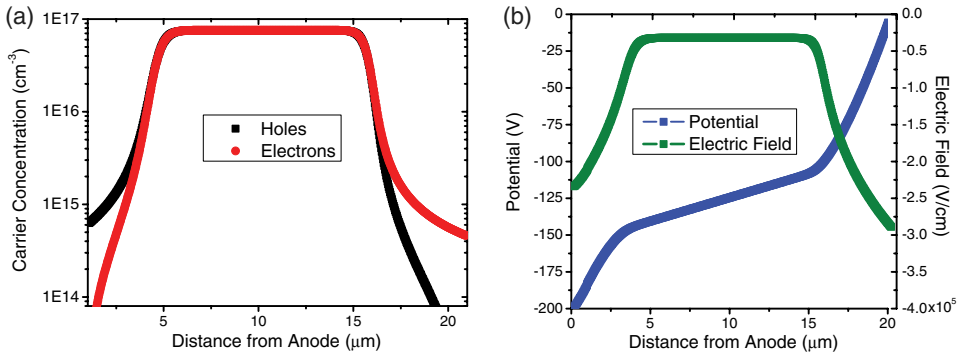

Fig. 2 (a) Carrier concentration as a function of position for a numerically simulated 20-μm lateral BHJ device under uniform illumination. (b) Simulated electric field and potential profile for the same 20-μm lateral BHJ device.

Table 1 Silvaco simulation parameters.

	Symbol	Simulation parameter	Value	Units
Organic transport parameters				
Zero field mobility	μ_{n0}	mun0	1.65×10^{-4}	$cm^2/(V*s)$
	μ_{p0}	mup0	1.90×10^{-4}	
Carrier lifetime	τ	taun0, taup0	1.00×10^{-5}	s
Bimolecular recombination coefficient	β	copt	1.05×10^{-12}	cm^3/s
Poole-Frenkel temperature-dependent factor	γ_n	e0n.pfmob	10,000	V/cm
	γ_p	e0p.pfomb	8264.5	
	(Γ_n)		(0.0010)	$(\sqrt{m/V})$
	(Γ_p)		(0.0011)	
Saturation velocity	v_{sat}	vsatn, vsatp	1.00×10^5	cm/s
Effective mass (for tunneling)	m_{tun}	me.tunnel, mh.tunnel	100	
Organic electronic and optical properties				
Bandgap	E_g	eg300	0.80	eV
Electron affinity	E_{ea}	affinity	4.2	eV
Electronic density of states	$N_{c,v}$	nc300, nv300	1.0×10^{21}	cm^{-3}
Relative permittivity	ε	permi	3.40	
Generation rate	G	(set in user-defined file)	6.00×10^{21}	$cm^{-3}\,s^{-1}$
Metal contact parameters				
Cathode work function	W_c	workf	4.2	eV
Anode work function	W_a	workf	5.0	eV

studies of lateral BHJ devices, either from detailed potential profiles or extrapolation from measurements within RZ.

The J-V characteristics of a lateral BHJ device can be described by a modified version of the equation for bipolar carrier extraction from an SCL material,

$$J_{\text{photo}} = \chi(4\varepsilon\mu)^{1/4}(qG)^{3/4}V^{1/2}, \tag{6}$$

where χ is a constant coefficient related to the carrier mobility ratio, μ is the mobility of the slower carrier, ε is the dielectric constant, q is the fundamental charge, G is the generation rate, V is the applied voltage bias, and J_{photo} is the lateral photocurrent density. This equation is derived from Eqs. (1) to (4) and is an adaptation of Eq. (15) reported in Ref. 11, for the SCL photocurrent in a unipolar lateral device. The modification here arises from the extension to the ambipolar case. The parameter χ ranges from 1 in the completely unipolar case to 1.4 for the case of equal carrier mobilities. The relationship between the mobility ratio and the parameter χ is explored in more detail in Fig. 7 of Ref. 18. Equation (6) also assumes that the voltage drop across the recombination zone is negligible, which can be seen in Fig. 2(b). Under the conditions of a large voltage drop within the RZ, Eq. (6) can be modified to

$$J_{\text{photo}} = \chi(4\varepsilon\mu)^{1/4}(qG)^{3/4}(V + E_r d)^{1/2}, \tag{7}$$

where E_r is the RZ electric field and d is the channel length. The RZ field is opposite in sign to the applied bias. Larger lateral BHJ devices with channel lengths $>5\ \mu$m typically have a

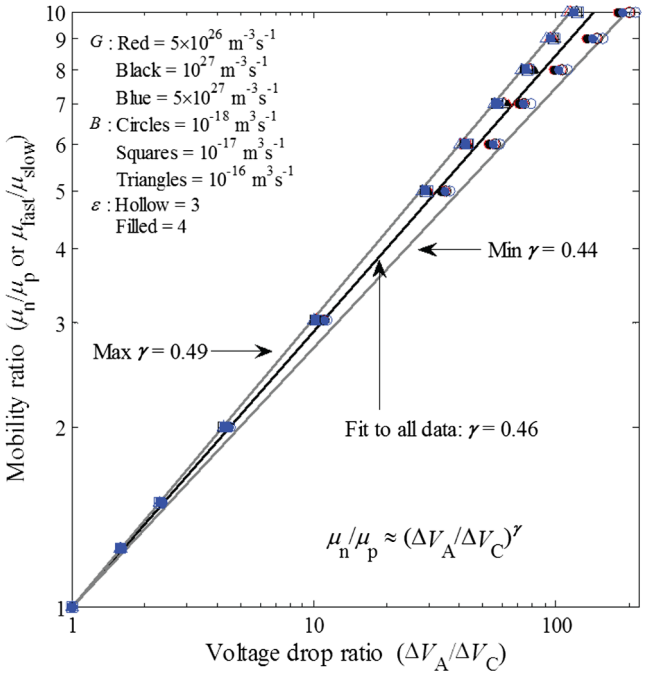

Fig. 3 Carrier mobility ratio versus the voltage drop across the space charge regions (SCRs) plotted for a variety of mobilities, generation rates, recombination coefficients, and relative permittivities. Reproduced with permission from Ref. 18.

significant RZ field and photocurrent described by Eq. (7). Within the RZ, the J-V behavior should be ohmic.

These SCL photocurrent conditions and distinct charge transport zones, however, are not present under all conditions in lateral BHJ devices. The functional form of their photocurrent versus voltage relationship varies depending on the applied electric field. This has been analyzed in measurements of lateral BHJ devices by calculating the slope of the lateral photocurrent density versus the voltage curve on a log-log plot. The slope (m) is the exponent in the dependent relationship $J_{\text{lat}} \propto V^m$. The change in this dependence with total applied bias (normalized to device length) is shown in Fig. 4. Measurements under reverse bias conditions are used to simulate the internal electric field during OPV operation and minimize carrier injection.[14] At low-bias voltages, less

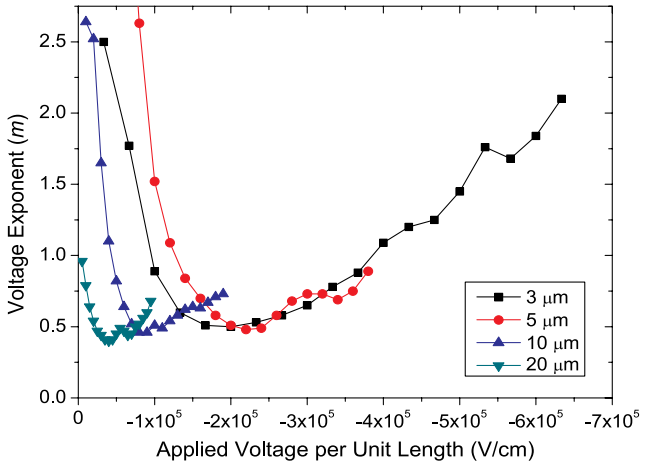

Fig. 4 Voltage exponent (m) versus applied voltage per unit length for lateral BHJ devices with channel lengths ranging from 3 to 20 μm. The voltage exponents are calculated using photocurrent versus applied bias measurements from P3HT:PCBM lateral BHJ devices under AM1.5 illumination. Reproduced with permission from Ref. 14.

than -1.0×10^5 V/cm, there are significant energetic barriers to carrier extraction, leading to large voltage exponents. With increasing applied bias, the exponent magnitude decreases until it stabilizes to ~0.5 in the range of $\sim -1.0 \times 10^5$ to -3.0×10^5 V/cm. This indicates the regime where SCL behavior is present. The voltage exponent is not always stable at 0.5 and does increase slightly at higher biases, due to the inability of the electrodes to completely block charge injections.[21] As the applied voltage increases in magnitude, there is a substantial current injection into the device, and it no longer exhibits well-defined SCL behavior as the voltage exponent rises. This preliminary analysis is necessary in order to isolate the regime in which our device model and the resulting analytical equations are valid.

3 Methods

3.1 *Simulations and Photoconductive Gain*

Photocurrents from organic BHJ lateral devices were simulated using the ATLAS® 2-D device simulator from Silvaco. This simulator, as described above, is based on the Poisson and drift-diffusion equations for lateral BHJ conditions, but models bimolecular recombination and the carrier mobilities as having a Poole-Frenkel dependence on an electric field. Using the "model" statement, bimolecular recombination and Poole-Frenkel mobility modeling were initiated using the "optr" and "pfmob" flags, respectively. The bimolecular recombination coefficient (copt) was 1.046×10^{21} and specified under the "material" statement. To model Poole-Frenkel field-dependent mobility, the temperature-dependent factors, "e0n.pfmob" and "e0p.pfmob", used were set to 10,000 and 8264.5 V/cm, also under the "material" statement. Additional modeling parameters, such as zero field mobility and generation rate, used are listed in Table 1; otherwise, the model used default parameter values for the organic material system. The work functions of the electrodes have been aligned with the energy levels of the BHJ to remove barriers at the contact interface in the simulation. The simulation used the air mass 1.5 (AM1.5) spectrum given by ATLAS for the light source. For each device length, the model used a mesh in the device channel with 300 nodes along the x axis. The resulting photocurrent at different applied reverse biases and light intensities was compared with experimental measurements from lateral BHJ devices.

Lateral BHJ devices with Al and Au contacts were fabricated on a glass substrate using photolithography [Fig. 1(a)]. These metals were chosen to reduce the barrier formed at the metal-semiconductor interface. The metal contacts were deposited using thermal evaporation to a thickness of 500 Å, with channel lengths ranging from 4 to 20 μm with a constant W/L = 1000. Before the deposition of the BHJ layer, the substrate was dipped into a phosphoric acid solution for 10 s to remove excess oxide from the surface of the Al electrodes. This was followed by a solvent rinse procedure of acetone, methanol, and isopropyl alcohol. The BHJ absorber layer was deposited from a 20-mg/mL solution of poly(3-hexylthiophene) (P3HT): phenyl-C61-butyric acid methyl ester (PCBM) (1:1 by weight) in 1,2-dichlorobenzene that had been heated to 70°C and stirred for over 12 h. The BHJ was spun-cast at 1200 rpm for 60 s, followed by annealing at 140°C for 15 min in a nitrogen atmosphere. The BHJ film was measured to be 100 nm thick. The measured BHJ layer thickness and electrode heights were used in the Silvaco photocurrent simulation.

Electrical measurements were performed in a Desert Cryogenics cryogenic probe station under vacuum better than 5×10^{-3} torr at 300 K using an Agilent 4155C semiconductor parameter analyzer. Current versus voltage characteristics were measured in the dark and under illumination. The sample illumination was achieved using an Oriel model 66912 and 66907 150-W ozone-free xenon lamp. The optical spectrum was modified using an AM1.5 spectral filter, and the light intensity was 100 mW/cm^2. Neutral density filters were used to modify the incident light intensity for photoconductive gain experiments.

3.2 *In Situ Potentiometry*

The fabrication and measurement procedure for the 20-μm channel length device and the devices used for photocurrent versus channel length studies have been described previously.[12,17] New

devices on glass substrates [Fig. 1(b)] were fabricated using the following procedure. Interdigitated electrodes and voltage probes were defined using a JEOL JBX-6000 electron beam lithography tool. The potentiometry device channel lengths were 50 μm with a W/L of 500, while the smaller devices had channel lengths of 3 μm with a W/L of 1000. Five nickel (Ni) probes extended 150 μm into the channel of the larger devices and were 200 nm wide. These voltage probes were placed at least 5 μm from the electrodes and 10 μm apart from each other inside the RZ of the large channel device. Al was used as the cathode, Au as the anode, and Ni for the voltage probes and device pads, due to its mechanical robustness. All metal layers were deposited via thermal evaporation to a thickness of 500 Å.

The substrate was cleaned in the same manner as described above. The BHJ absorber layer was deposited from a 20-mg/mL solution of P3HT:PCBM (1 : 1 by weight) in chloroform that had been heated to 50°C and stirred for >16 h. The BHJ was spun-cast at 1200 rpm for 60 s, followed by annealing at 140°C for 15 min in a nitrogen atmosphere.

The sample measurement and illumination were achieved using the same procedure and setup as for the experiments on photoconductive gain detailed above. Current versus voltage characteristics were measured in the dark and under illumination, while *in situ* potentiometry was performed simultaneously using the Ni probes in the channel. The electric field generated due to the work function differences between electrodes and Ni probes were negligible compared to the overall field acting on the charge carriers within the lateral BHJ structure.

3.3 *EFISH Microscopy*

Electric field induced second harmonic generation (EFISH) microscopy is a special case of second harmonic generation in which the efficiency of converting two photons of frequency ω to one photon of frequency 2ω is determined by the strength of the electric field in the system. Under illumination by a fundamental laser beam, lateral BHJ devices generate photocurrent via two-photon absorption. All second harmonic intensity is polarized in the direction along the channel so that the intensity is proportional to the square of the applied electric field. The exact proportionality constant is calculated on a log-log plot of the integrated square root of the second harmonic intensity and the bias voltage. Details on EFISH microscopy fundamentals can be found in previously published work.[22,23] A laser pulse energy was selected so as to generate an average photocurrent density equivalent to that generated under AM1.5 illumination.

Lateral BHJ devices for EFISH microscopy were fabricated on glass substrates with gold and aluminum electrodes, both 50 nm thick. The channel length of these devices was 15 μm. Before spin coating, samples were cleaned using a phosphoric acid etch and solvent rinse, as described above. A variety of P3HT:PCBM and PSBTBT:PCBM solutions were prepared to observe the effect of the BHJ solution recipe on the internal electric field of the lateral device. The P3HT:PCBM recipe can be found in Ref. 22 and the PSBTBT:PCBM recipes in Ref. 23. All devices were encapsulated with a microscope coverslip and epoxy, and then cured at 125°C for 10 min. All microscopy images were taken in the transmission mode and under an applied reverse bias of 200 V. The exact experimental setup has been described in detail in previous publications.[22,23]

4 Results

4.1 *Photocurrent Versus Device Length*

An important feature of lateral BHJ devices is the ease at which their channel length can be modified, in order to examine charge transport over a wide range of length scales. The photocurrent versus device length from P3HT:PCBM lateral BHJ devices with channel lengths ranging from 100 nm to 20 μm is shown on a log-log scale in Fig. 5. These devices were measured under AM1.5 illumination and reverse bias conditions to achieve electric field strengths similar to those inside OPV cells. The photocurrent increases as a function of reverse bias and device length until ~5 μm. Previous studies have shown that SCR lengths in these materials under the experimental conditions range from 2 to 5 μm.[24] The majority of carriers that are photogenerated

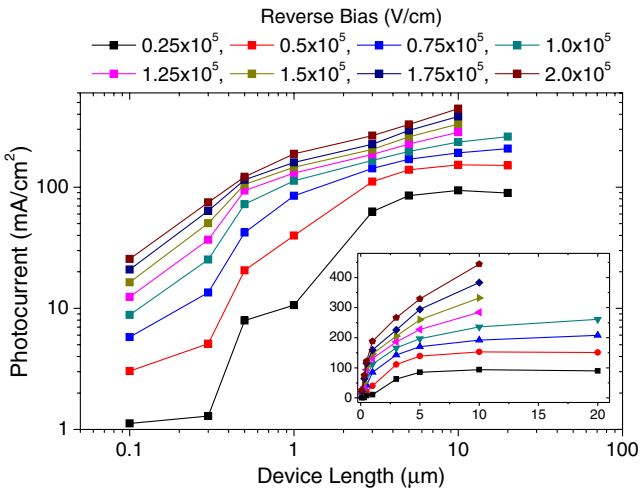

Fig. 5 Photocurrent versus device length (log-log scale) for P3HT:PCBM lateral BHJ devices. Inset: photocurrent versus device length (linear) for the same devices. Reproduced and modified with permission from Ref. 17.

in the SCRs will be efficiently extracted and will contribute to the measured photocurrent. Therefore, increases in the device channel length up to this point will have a significant effect on the photocurrent. In larger channel length devices, the size of the SCRs remains the same and only the RZ significantly increases in size, which does not contribute to the photocurrent. This is shown in the inset of Fig. 5, where the photocurrent and device length are plotted on a linear scale. Beyond a device length of 5 μm, the photocurrent saturates as the additional photogenerated carriers are formed in the RZ of the larger devices. At higher field strengths, the photocurrent saturation is less pronounced due to an additional contribution to the photocurrent from injection, as indicated in the voltage exponent plot. These trends support the existence of SCRs and an RZ within lateral BHJ devices and their behavior as described in the theory section.

4.2 *In Situ Potentiometry*

Voltage probe measurements on lateral BHJ devices yield linear voltage sweeps throughout the applied bias range. Measurements from a particular applied reverse bias can be plotted spatially to construct the channel voltage profile, as in Fig. 6. The slope of the potential profile is the

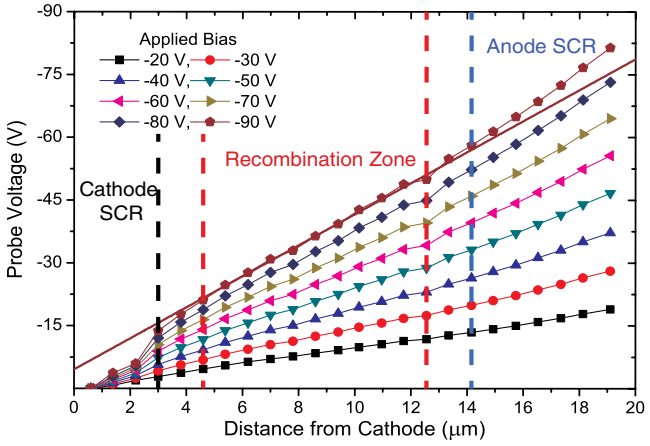

Fig. 6 Potential profiles of a lateral P3HT:PCBM device under 96 mW/cm^2 AM1.5 illumination. The demarcation of the different zones is based on voltage exponent analysis. The projected line from the recombination zone (RZ) shows the increased electric field in the SCRs. The axis intercepts of this projected line indicate the voltage drops across the cathode and anode SCRs. Reproduced with permission from Ref. 12.

magnitude of the electric field in the channel. This profile is similar to the simulated profile in Fig. 2(b) with increased electric field strength close to the contacts in the SCRs. We can determine the extent of the three regions within the channel by performing the voltage exponent analysis using the potentiometric measurements from any two voltage probes. The current is continous throughout the device. SCL behavior, with an exponent m close to 0.5, is observed from 0 to 3 μm and 14.1 to 20 μm, defining the extent of SCRs.[12] The larger SCR adjacent to the anode indicates that holes are the slower carrier within the BHJ. A voltage exponent close to 1, consistent with the ohmic behavior predicted in the RZ, is observed from 4.6 to 12.6 μm within the device channel. Although resolution is limited due to the lithographic constraints of probe fabrication, this technique is capable of determining the approximate extents of the different regions and confirming that different charge transport mechanisms are prevalent within different areas of the device.

The carrier mobility ratio in a BHJ material is calculated from the potential profile using Eq. (5). In Fig. 6, the projected line indicates E_r, the RZ field, at an applied bias of −90 V. The intercepts of this line at 0 and 20 μm, the locations of the contacts, indicate the voltage drops across the two SCRs. A larger voltage drop across the anode SCR is due to the holes being the slower carriers; this is consistent with the larger anode SCR length. From Eq. (5), the carrier mobility ratio is ∼1.50. This calculation was repeated for the different applied biases in Fig. 6 and is consistent over this range. As the RZ field in this device is large, Eq. (7) is used to calculate the slower hole mobility from the measured photocurrent. The electron mobility can now be found from the previously calculated mobility ratio. The resulting mobility values of $\mu_h = 3.65 \times 10^{-4}$ cm^2/Vs and $\mu_e = 5.49 \times 10^{-4}$ cm^2/Vs are comparable with literature values for vertical solar cells.[25,26]

From the two carrier mobilities, we can also calculate the carrier concentration and bimolecular recombination coefficient for these BHJ materials. As the electron and hole carrier concentrations are equal in the RZ, the conductivity within this region can be defined as

$$\frac{J_{\mathrm{ph}}}{E_r} = e\Delta n(\mu_h + \mu_e) = e\sqrt{\frac{G}{B}}(\mu_h + \mu_e), \tag{8}$$

where Δn is the electron (or hole) concentration in the RZ and B is the bimolecular recombination coefficient. Bimolecular recombination within these materials is supported from the relationship between the conductivity and the incident light intensity.[12,17] Similar to earlier reports on vertical P3HT:PC$_{61}$BM solar cells,[26,27] the bimolecular recombination coefficient is orders of magnitude smaller than the Langevin recombination coefficient; in this case, B/B_L is ∼0.0068. *In situ* potentiometry measurements on lateral devices can, therefore, be used to find several important parameters within BHJ materials, listed in Table 2.

Constructing a detailed potential profile using *in situ* potentiometry as in Fig. 6, however, is difficult and time consuming. This procedure can be simplified by only probing a few points in the center of the device to measure the RZ field and measure the voltage drops across the SCRs. A simplified potential profile for a P3HT:PCBM lateral BHJ device is shown in Fig. 7. As before, the presence of SCL behavior and the location of the voltage probes within the RZ were confirmed using voltage exponent analysis. The projected lines from the potential profiles indicate the voltage drops across the SCRs, and using Eq. (5), a mobility ratio of 0.63 with holes is the faster carrier. The slower electron mobility is calculated from photocurrent measurements on smaller channel length devices using Eq. (6). Carrier concentrations and recombination coefficients are then calculated using the method described above. This simplified procedure greatly reduces the measurement time and can be used to actively monitor the change in charge transport parameters in BHJ materials in response to environmental conditions. The potentiometry

Table 2 Charge transport parameters of the lateral bulk heterojunction (BHJ) device from Fig. 6 under 96 mW cm^{-2} AM1.5 illumination. Reproduced with permission from Ref. 12.

μ_h (cm^2 V^{-1} s^{-1})	μ_e (cm^2 V^{-1} s^{-1}	Δn (cm^{-3})	B_r (cm^3 s^{-1})
3.65×10^{-4}	5.49×10^{-4}	2.34×10^{16}	1.13×10^{-11}

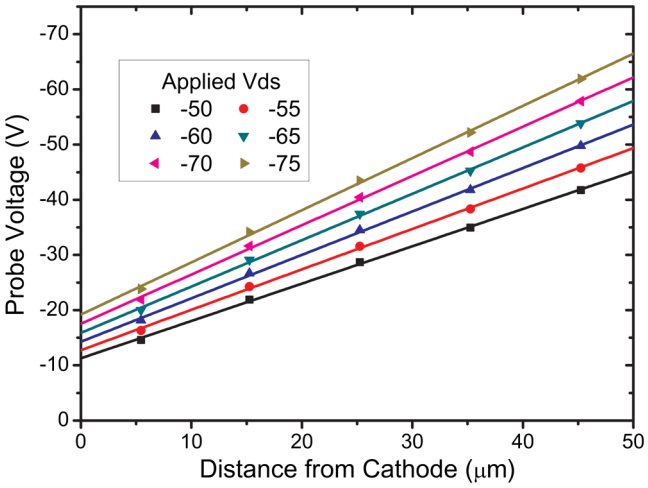

Fig. 7 Potential profiles of a lateral P3HT:PCBM device under 96 mW cm^{-2} AM1.5 illumination, taken at $t = 60$ min. All voltage probe measurements lie within the RZ of these devices; therefore, the fitted lines indicate the RZ field, E_r. The intercepts of this projected line at 0 and 50 μm indicate the voltage drops across the cathode and anode SCRs.

measurements were performed multiple times while the sample was under vacuum, but subject to AM1.5 illumination. We assumed that the faster hole mobility remained constant, as the mobility ratio consistently decreased with time. Table 3 lists the charge transport parameters of the P3HT:PCBM film at multiple times relative to the beginning of the measurement. These values are consistent with previous reports using photo-CELIV and SCL-based methods.[13,28–30]

The carrier mobility imbalance increases with time, while the RZ conductivity was observed to decrease, indicating a lower carrier concentration and a higher bimolecular recombination coefficient. This experiment was repeated after 1,8-diiodooctane (DIO) was added to the P3HT:PCBM solution to observe the effect of the solvent additive on the degradation process. DIO is known to produce better phase separation and structural order within BHJ films, resulting in the higher performance of OPV cells.[31,32] The addition of DIO did not eliminate the mobility imbalance in favor of holes or the decreasing trend of the mobility ratio, but the carrier mobilities and other parameters improved. The details of this experiment will be published in an upcoming manuscript. This simplified technique utilizing lateral BHJ devices offers a unique method to monitor degradation within the BHJ film and relate degradation to changes in the charge transport parameters.

In most disordered organic semiconductors, there is an electric field dependence of carrier mobility; *in situ* potentiometry is also capable of evaluating this relationship. Figure 8(a) plots the measured photocurrent versus the combined SCR voltage drop from a 10-μm P3HT:PCBM lateral device. The analysis technique described above was used to calculate an electron mobility of 3.8×10^{-4} cm^2/Vs and a hole mobility of 4.6×10^{-4} cm^2/Vs.[18] These values were extracted from a fit to Eq. (7), shown as a solid line in Fig. 8(a) over the range in which SCL transport was observed. However, the experimental photocurrent curve has a steeper gradient than what is predicted by the theoretical straight line. This may be caused by a small increase in carrier mobilities with an increasing electric field. We calculate a series of best fit lines from Eq. (7) with

Table 3 Charge transport parameters of a lateral P3HT:PCBM device under 96 mW cm^{-2} AM1.5 illumination.

P3HT:PCBM	μ_n/μ_p	μ_p (cm^2 V^{-1} s^{-1})	μ_n (cm^2 V^{-1} s^{-1})	Δn (cm^{-3})	B_r (cm^3 s^{-1})
0 min	0.76	4.08×10^{-4}	3.10×10^{-4}	2.22×10^{17}	1.26×10^{-13}
30 min	0.69	4.08×10^{-4}	2.81×10^{-4}	1.81×10^{17}	1.88×10^{-13}
60 min	0.63	4.08×10^{-4}	2.57×10^{-4}	7.72×10^{16}	1.04×10^{-12}

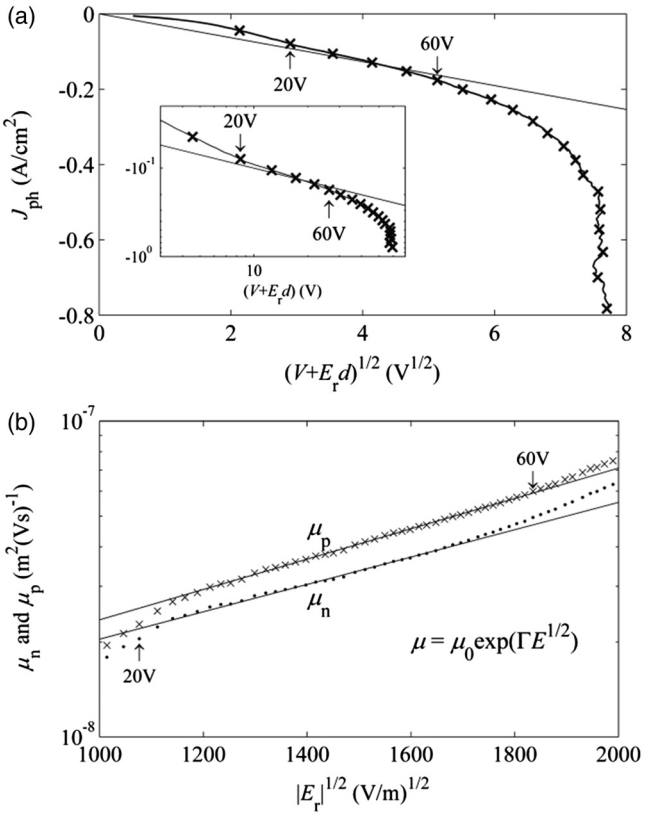

Fig. 8 (a) Measured photocurrent of a 10-μm lateral P3HT:PCBM device versus $(V + E_r d)^{1/2}$. The solid line is a linear fit to Eq. (3) over the range in which SCL behavior is observed. The inset shows the same data and fit, but in a double-logarithm plot. (b) Plot of electron (•) and hole (×) mobilities versus the RZ electric field for the bias range of 20 to 60 V. The solid lines are best fit lines according to the Poole-Frenkel model. Reproduced with permission from Ref. 18.

different, increasing slopes over the entire voltage range from 20 to 60 V to obtain the change in carrier mobilities. If we consider that the recombination zone occupies the majority of the device length, then most charge carriers within the device experience an electric field similar to the RZ electric field. The series of recalculated electron and hole mobilities over the voltage range from 20 to 60 V are plotted with the square root of the RZ field in Fig. 8(b). Data from within the SCL range is best fitted by the inset equation, based on the Poole-Frenkel model.

$$\mu = \mu_0 \exp\left(\Gamma\sqrt{|E_r|}\right), \tag{9}$$

where μ_0 is the zero field mobility and Γ is a temperature-dependent activation factor.[18] The close fit to the data suggests the Poole-Frenkel-like transport behavior in the lateral direction for P3HT:PCBM. We extract zero field mobilities of 7.8×10^{-5} and 7.5×10^{-5} cm^2/Vs for holes and electrons, respectively.[18]

4.3 *EFISH Microscopy*

Rapid degradation within BHJ films can also be monitored using EFISH microscopy. As explained above, the intensity of a second harmonic light generation within the BHJ system can be used to determine the local electric field strength and, therefore, the potential profile. EFISH microscopy images are shown in the inset of Fig. 9(a), along with their corresponding electric field profiles. The initial electric field distribution indicates the presence of a hole-dominated SCR due to the field enhancement adjacent to the anode. A small electron-dominated SCR

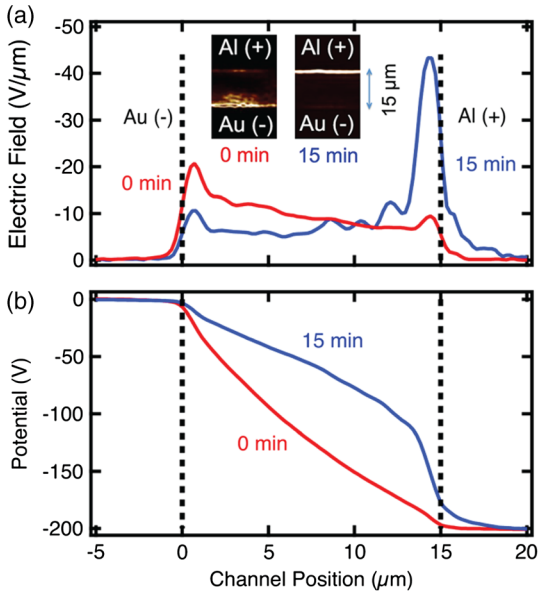

Fig. 9 (a) The electric field distribution across the P3HT:PCBM channel obtained within the first 1 min of laser exposure (red) and after 15 min of laser exposure (blue). The inset shows EFISH microscopy images obtained on the two time scales for the P3HT:PCBM device with a bias voltage of −200 V. (b) Electric potential profiles corresponding to the electric fields shown in (a). Reproduced with permission from Ref. 22.

may also be present at these initial conditions. However, after 15 min under laser illumination, the electric field magnitude adjacent to the cathode significantly increases. This change is also seen in the potential profiles constructed from the electric field profile data [Fig. 9(b)]. The initial linear potential profile (red) becomes highly nonlinear at 15 min, with a significant voltage drop near the cathode. Over a short period of time, the carrier mobilities become highly asymmetric. The formation of this electron-dominated SCR is consistent with a rapid decrease in the electron mobility. Previous measurements have suggested that photo-oxidation introduces negatively charged electron traps adjacent to the cathode in P3HT:PCBM devices.[33] This may be caused by moisture trapped inside the sealed device. Similar EFISH measurements on PSBTBT:PCBM films did not shown rapid SCR formation, suggesting that these materials may be more resilient to environmental degradation.[22]

EFISH can also be used to measure actual charge carrier concentrations within different device regions, utilizing the differential form of Gauss's law

$$\frac{dE_x}{dx} = \frac{q}{\varepsilon}[p(x) - n(x)], \tag{10}$$

where x is the direction across the channel. To quantify the charge collection, a best fit line was applied to the measured EFISH electric field profiles, and the slope was taken as the average derivative throughout each region. The amount of excess carriers in different regions of PSBTBT:PCBM lateral devices are shown in Table 4.

Table 4 The magnitude and carrier type of each space charge accumulation region in PSBTBT:PCBM devices with different BHJ recipes. Reproduced with permission from Ref. 23.

	Accumulation ($\times 10^{14}$ cm^{-3}) of electrons or holes		
	0.5 to 4.0 μm	4.0 to 16.0 μm	16.0 to 19.5 μm
3:1 PSBTBT:PCBM	$2.1 \pm 0.9\,h^+$	$\mathbf{0.5 \pm 0.02}\,e^-$	$\mathbf{2.8 \pm 0.2}\,e^-$
1:3 PSBTBT:PCBM	$5.5 \pm 1.1\,h^+$	$1.6 \pm 0.03\,h^+$	$\mathbf{0.5 \pm 0.2}\,e^-$

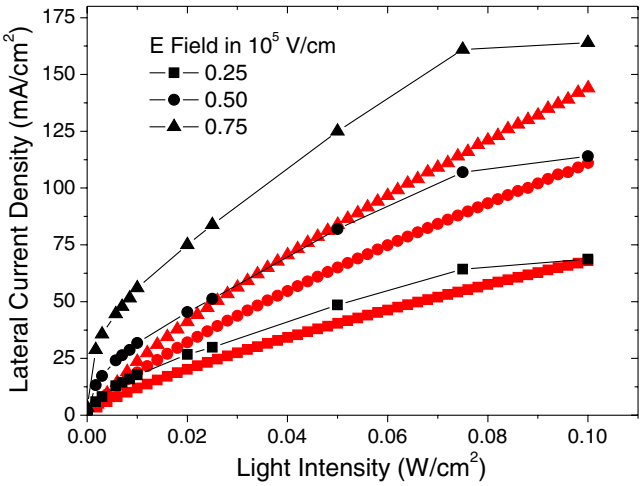

Fig. 10 Comparison between simulated (red) and experimental (black) lateral current density versus incident light intensity behavior for a 5-μm channel length P3HT:PCBM lateral device.

As expected from the three-zone model, excess carrier concentrations are observed adjacent to the electrodes, with excess holes close to the anode and excess electrons close to the cathode. A reduction in the PSBTBT concentration should result in a lower hole mobility and, therefore, a higher hole concentration in the anode SCR. Conversely, a reduced PCBM concentration should result in a higher electron concentration in the cathode SCR due to the lower electron mobility. This is supported by the EFISH measurements. The lower hole mobility in the 1:3 PSBTBT:PCBM solution results in high hole accumulation at the anode, while the 3:1 PSBTBT:PCBM recipe leads to roughly equal hole and electron concentrations in the two SCRs. This indicates that the mobilities in the 3:1 recipe are less mismatched than in the 1:3 recipe. The high imbalance in carriers in the 1:3 PSBTBT:PCBM device suggests that this recipe approaches the unipolar regime with only a single carrier accumulating.[18] The space charge accumulation is consistently lower in the central region; although the individual carrier concentrations are high in the RZ, they are roughly equal, leading to a reduced electric field. There is still some charge accumulation in the central region, which suggests that charge collection occurs even over large distances of up to 10 μm. This is consistent with previous scanning photocurrent measurements that have shown some charge collection from the center of 20-μm PSBTBT:PCBM lateral devices.[17,24]

4.4 *Photoconductive Gain*

Lateral BHJ devices have also been used to study photoconductive gain. The lateral photocurrent density versus incident light intensity on a 5-μm P3HT:PCBM device is shown in Fig. 10. These devices were measured under a range of illumination conditions and compared with simulated photocurrent using Silvaco's Atlas 2-D program. The experimental and simulation results closely track each other at lower applied bias voltages. Photoconductive gain is primarily seen at low light intensities and at the highest applied electric fields as a rapid increase in the experimental photocurrent density. Dark current injection from the electrodes is the source of this gain. It is not seen in the simulated photocurrent due to the imposed metal work function and organic energy band alignment in the model. The details of this work will be published in an upcoming manuscript.

5 Conclusion

In this review, we have described the key optoelectronic properties of lateral BHJ devices and demonstrated their use as materials diagnostic platforms. These devices exhibit space charge limited transport behavior under steady-state conditions similar to those of a conventional OPV cell. A detailed computational model is presented to describe the potential, electric

field, and carrier concentration profiles of lateral BHJ devices, as well as the current versus voltage characteristics of different regions of the device. This model has been confirmed by a variety of experimental techniques. SCRs dominated by the slower carrier exist over several microns in lateral BHJ devices. By fabricating devices with channel lengths over a wide range of values, we show evidence for long drift lengths in organic BHJ materials of up to 5 μm from their SCL behavior. In larger devices, two SCRs form adjacent to the electrodes separated by a central zone where recombination is dominant. The voltage across these SCRs depends on the carrier mobility ratio through an empirically derived relation. *In situ* potentiometry is used to construct detailed potential profiles of the channel and calculate carrier mobilities as well as the carrier concentration and bimolecular recombination coefficient in the bulk material. A simplified *in situ* potentiometry and photocurrent measurement technique can also be used to calculate the mobility ratio and monitor changes in charge transport parameters due to environmental effects, such as degradation. EFISH, a nonlinear optical microscopy technique, is used to measure the electric field and carrier concentrations within the device channel. These independent measurements confirm our three-zone model and also allow observation of rapid degradation within the film. Lateral device structures are a useful diagnostic platform for a variety of measurement techniques to characterize charge transport in BHJ materials. These techniques offer a useful complement to measurements on vertical photovoltaic structures and provide a more complete and detailed picture of OPV materials.

Acknowledgments

The authors would like to thank the facilities staff at the Microelectronics Research Center at the University of Texas at Austin. E. Danielson and A. Dodabalapur would like to acknowledge the ONR under STTR Project No. 00014-10-M-0317 and Z. Ooi acknowledges funding provided by A*STAR under the visiting investigator program (VIP). A. Dodabalapur and C. Lombardo also acknowledge the program "Understanding Charge Separation and Transfer at Interfaces in Energy Materials (EFRC:CST)," an Energy Frontier Research Center funded by the U.S. Department of Energy, Office of Science, Office of Basic Energy Sciences under Award Number DE-SC0001091. We thank Konarka Technologies for providing the PSBTBT polymer sample.

References

1. M. A. Green et al., "Solar cell efficiency tables (version 42)," *Prog. Photovoltaics: Res. Appl.* **21**(5), 827–837 (2013).
2. S. R. Cowan, A. Roy, and A. J. Heeger, "Recombination in polymer-fullerene bulk heterojunction solar cells," *Phys. Rev. B* **82**(24), 245207 (2010).
3. R. Osterbacka et al., "Mobility and density relaxation of photogenerated charge carriers in organic materials," *Curr. Appl. Phys.* **4**(5), 534–538 (2004).
4. A. J. Morfa et al., "Time-of-flight studies of electron-collection kinetics in polymer: fullerene bulk-heterojunction solar cells," *Adv. Funct. Mater.* **21**(13), 2580–2586 (2011).
5. T. M. Clarke et al., "Non-Langevin bimolecular recombination in a silole-based polymer: PCBM solar cell measured by time-resolved charge extraction and resistance-dependent time-of-flight techniques," *Energy Environ. Sci.* **5**(1), 5241–5245 (2012).
6. J. V. Li et al., "Simultaneous measurement of carrier density and mobility of organic semiconductors using capacitance techniques," *Org. Electron.* **12**(11), 1879–1885 (2011).
7. W. L. Leong, S. R. Cowan, and A. J. Heeger, "Differential resistance analysis of charge carrier losses in organic bulk heterojunction solar cells: observing the transition from bimolecular to trap-assisted recombination and quantifying the order of recombination," *Adv. Energy Mater.* **1**(4), 517–522 (2011).
8. X. Ai et al., "Photoinduced charge carrier generation in a poly(3-hexylthiophene) and methanofullerene bulk heterojunction investigated by time-resolved terahertz spectroscopy," *J. Phys. Chem. B* **110**(50), 25462–25471 (2006).
9. A. Baumann et al., "Influence of phase segregation on recombination dynamics in organic bulk-heterojunction solar cells," *Adv. Funct. Mater.* **21**(9), 1687–1692 (2011).

10. K. K. H. Chan et al., "Charge injection and transport studies of poly(2,7-carbazole) copolymer PCDTBT and their relationship to solar cell performance," *Org. Electron.* **13**(5), 850–855 (2012).
11. Z. E. Ooi et al., "Analysis of photocurrents in lateral-geometry organic bulk heterojunction devices," *Appl. Phys. Lett.* **101**(5), 053301 (2012).
12. E. Danielson et al., "Bimolecular recombination coefficient calculation by in situ potentiometry in a bulk heterojunction organic photovoltaic material," *Appl. Phys. Lett.* **102**(17), 173304 (2013).
13. C. Lombardo et al., "Lateral mobility measurements in organic bulk heterojunctions: comparison of field-effect and space charge mobilities," *J. Photonics Energy*, **2**(1), 021007 (2012).
14. C. Lombardo et al., "Electrical characteristics of lateral organic bulk heterojunction structures," *Org. Electron.* **13**(7), 1185–1191 (2012).
15. A. M. Goodman and A. Rose, "Double extraction of uniformly generated electron-hole pairs from insulators with noninjecting contacts," *J. Appl. Phys.* **42**(7), 2823–2830 (1971).
16. V. D. Mihailetchi, J. Wildeman, and P.W.M. Blom, "Space-charge limited photocurrent," *Phys. Rev. Lett.* **94**(12), 126602 (2005).
17. C. Lombardo et al., "Device physics and operation of lateral bulk heterojunction devices," *J. Phys. Chem. B* **117**(16), 4503–4509 (2013).
18. Z. E. Ooi et al., "Evaluating charge carrier mobility balance in organic bulk heterojunctions using lateral device structures," *J. Phys. Chem. C* (2014), in review.
19. B. Cobb et al., "Velocity-field characteristics of polycrystalline pentacene field-effect transistors," *J. Appl. Phys.* **107**(12), 124503 (2010).
20. L. Wang et al., "Electric-field-dependent charge transport in organic thin-film transistors," *J. Appl. Phys.* **101**(5), 054515 (2007).
21. V. D. Mihailetchi et al., "Cathode dependence of the open-circuit voltage of polymer:fullerene bulk heterojunction solar cells," *J. Appl. Phys.* **94**(10), 6849–6854 (2003).
22. J. D. Morris et al., "Mapping electric field distributions in biased organic bulk heterojunctions under illumination by nonlinear optical microscopy," *Appl. Phys. Lett.* **102**(3), 033301 (2013).
23. J. D. Morris et al., "Quantifying space charge accumulation in organic bulk heterojunctions by nonlinear optical microscopy," *Org. Electron.* **14**(11), 3014–3018 (2013).
24. C. Lombardo et al., "Scanning photocurrent microscopy of lateral organic bulk heterojunctions," *Phys. Chem. Chem. Phys.* **14**(38), 13199–13203 (2012).
25. A. J. Mozer et al., "Charge carrier mobility in regioregular poly(3-hexylthiophene) probed by transient conductivity techniques: a comparative study," *Phys. Rev. B* **71**(3), 035214 (2005).
26. G. Sliauzys et al., "Recombination of photogenerated and injected charge carriers in pi-conjugated polymer/fullerene blends," *Thin Solid Films* **511–512**, 224–227 (2006).
27. C. Deibel, A. Baumann, and V. Dyakonov, "Polaron recombination in pristine and annealed bulk heterojunction solar cells," *Appl. Phys. Lett.* **93**(16), 163303 (2008).
28. V. Chellappan et al., "Imbalanced charge mobility in oxygen treated polythiophene/fullerene based bulk heterojunction solar cells," *Appl. Phys. Lett.* **95**(26), 263305 (2009).
29. D. Chirvase et al., "Electrical and optical design and characterisation of regioregular poly(3-hexylthiophene-2,5diyl)/fullerene-based heterojunction polymer solar cells," *Synth. Met.* **138**(1–2), 299–304 (2003).
30. A. Pivrikas et al., "A review of charge transport and recombination in polymer/fullerene organic solar cells," *Prog. Photovoltaics: Res. Appl.* **15**(8), 677–696 (2007).
31. J. T. Rogers et al., "Structural order in bulk heterojunction films prepared with solvent additives," *Adv. Mater.* **23**(20), 2284–2288 (2011).
32. B. A. Collins et al., "Absolute measurement of domain composition and nanoscale size distribution explains performance in PTB7:PC71BM solar cells," *Adv. Energy Mater.* **3**(1), 65–74 (2013).
33. A. Seemann et al., "Reversible and irreversible degradation of organic solar cell performance by oxygen," *Sol. Energy* **85**(6), 1238–1249 (2011).

Eric Danielson received his BS degree in physics from Trinity University in San Antonio, Texas, in 2007 and his master's in physics from the University of Florida at Gainesville, Florida, in 2008. He is currently a PhD candidate in materials science and engineering at the University of Texas at Austin, studying charge transport in organic bulk heterojunction photovoltaic materials.

Zi-En Ooi received his MEng degree in chemical engineering and his PhD in chemistry from Imperial College London in 2004 and 2008, respectively. He remained at Imperial until 2009, when he joined the Institute of Materials Research and Engineering, Agency for Science, Technology and Research (A*STAR) in Singapore. His main research interest lies in organic and printed electronic devices, especially solar cells, but has forayed into areas such as electrochromics and microfluidics.

Kelly Liang is an undergraduate student in the Department of Electrical & Computer Engineering at the University of Texas at Austin, graduating in the spring of 2014. In the fall of 2014, she will begin graduate work toward a PhD in electrical engineering, simulating charge transport and recombination processes in photovoltaic materials.

Joshua Morris received his PhD in physical chemistry from the University of Texas at Austin in 2013. He is currently a postdoctoral researcher in the School of Chemistry and Biochemistry at the Georgia Institute of Technology. In the fall of 2014, he will begin an appointment as an assistant professor of chemistry at Georgia Gwinnett College.

Christopher Lombardo received his BS degrees in electrical engineering and physics from the University of Maryland in 2005 and his PhD in electrical engineering from the University of Texas at Austin in 2011 while studying charge transports and recombination mechanisms in bulk heterojunction photovoltaic materials. Since 2012, he has been employed by the Harvard School of Engineering and Applied Sciences.

Ananth Dodabalapur is an Ashley H. Priddy Centennial professor in engineering in the Department of Electrical & Computer Engineering at the University of Texas at Austin. He received his BS from the Indian Institute of Technology, Chennai, in 1985, and his MS and PhD degrees in electrical engineering from the University of Texas at Austin in 1987 and 1990, respectively. Between 1990 and 2001, he was with Bell Laboratories, Murray Hill, New Jersey.